Negative effective excitonic diffusion in monolayer transition metal dichalcogenides

Citation for the original published paper (version of record):
Rosati, R., Perea Causin, R., Brem, S. et al (2020). Negative effective excitonic diffusion in monolayer transition metal dichalcogenides. Nanoscale, 12(1): 356-363.
http://dx.doi.org/10.1039/c9nr07056g

Nanoscale

ROYAL SOCIETY OF CHEMISTRY

PAPER

View Article Online
View Journal | View Issue

Cite this: *Nanoscale*, 2020, **12**, 356

Negative effective excitonic diffusion in monolayer transition metal dichalcogenides†

Roberto Rosati, * Raül Perea-Causín, Samuel Brem and Ermin Malic

While exciton relaxation in monolayers of transition metal dichalcogenides (TMDs) has been intensively studied, spatial exciton diffusion has received only a little attention – in spite of being a key process for optoelectronics and having already shown interesting unconventional behaviours (*e.g.* spatial halos). Here, we study the spatiotemporal dynamics in TMD monolayers and track optically excited excitons in time, momentum, and space. In particular, we investigate the temperature-dependent exciton diffusion including the remarkable exciton landscape constituted by bright and dark states. Based on a fully quantum mechanical approach, we show at low temperatures an unexpected *negative effective diffusion* characterized by a shrinking of the spatial exciton distributions. This phenomenon can be traced back to the existence of dark exciton states in TMD monolayers and is a result of an interplay between spatial exciton diffusion and intervalley exciton–phonon scattering.

Received 15th August 2019,
Accepted 20th November 2019

DOI: 10.1039/c9nr07056g

rsc.li/nanoscale

Monolayers of transition metal dichalcogenides (TMDs) have attracted much attention[1–14] in particular due to their remarkable exciton landscape including bright and momentum- and spin-dark exciton states.[1,6,8,12] Recently, their spatiotemporal exciton dynamics has been studied,[15–22] showing peculiar effects including a distinct diffusion of bright and spin-dark excitons at low temperatures[20] as well as the formation of spatial halos at higher excitation densities.[21] The latter has been suggested to stem from phonon winds[23] or efficient thermal drifts.[24]

In this work, we shed light on the impact of the versatile exciton landscape including bright and momentum-dark states on spatiotemporal exciton dynamics in TMD monolayers in different temperature regimes. The resulting evolution is a complicated process with the coexistence of several many-particle mechanisms, showing in particular the appearance of different phases which will be addressed in the following. At a more simplified level, one expects that after optical excitation the excitons thermalize in energy on a quick timescale of hundreds of femtoseconds at room temperature[10,11] [Fig. 1(a)]. However, spatial propagation can also result on longer timescales in anisotropic exciton occupations, since excitons with the same energy but different momentum orientation propagate towards different spatial directions – similarly to electrons in quantum wells.[25,26] Momentum thermalization at each space point drives toward an isotropic distribution [Fig. 1(b)]. During this evolution, the excitonic spatial distribution undergoes an *effective diffusion*, *i.e.* it broadens in space while preserving the position of the maximum distribution and rotational

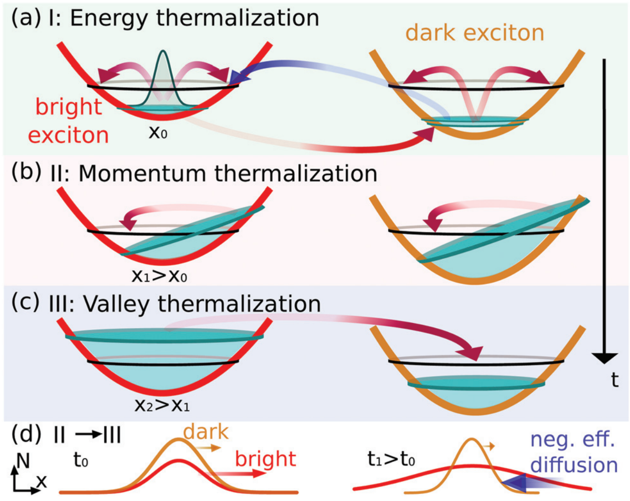

Fig. 1 Schematic illustration of spatiotemporal exciton dynamics in TMD monolayers. Effective exciton diffusion results in anisotropic distributions at different space points and in non-equilibrium distributions between bright and dark exciton states. As a result, the dynamics is characterized by three temporally subsequent phases describing (a) energy, (b) momentum, and (c) valley thermalization. The black circles visualize the equilibrium distribution and the arrows indicate exciton–phonon scattering channels. (d) Different exciton diffusion characteristics can result in apparent effective back-diffusion processes (blue arrow) that are necessary to establish spatial equilibrium distributions.

Chalmers University of Technology, Department of Physics, 412 96 Gothenburg, Sweden. E-mail: roberto.rosati@chalmers.se

† Electronic supplementary information (ESI) available. See DOI: 10.1039/C9NR07056G

symmetry. Here effective diffusion refers to the transient evolution, whereas the conventional diffusion refers to the steady-state regime.[18,20] Furthermore, different diffusion characteristics of bright and dark states can result in a local non-equilibrium among different valleys. Here, a space-dependent equilibration of bright and dark states leads toward a valley-thermalized occupation [Fig. 1(c)].

Based on a fully quantum mechanical approach,[10,11,14] this work provides microscopic insights into the interplay of spatiotemporal exciton dynamics and thermalization. We resolve the evolution of optically excited, spatially localized excitons in time, momentum, energy, and space taking into account bright and momentum-dark excitonic states. We predict unexpected spatiotemporal dynamics including the emergence of a negative effective diffusion, where the spatial profiles of the excitonic distribution shrink in space, apparently moving back towards the excitation center [*cf.* blue arrow in Fig. 1(d)].

1. Theoretical approach

Our goal is to study on a microscopic footing the spatiotemporal dynamics of excitons in the exemplary hBN-encapsulated tungsten disulfide (WS_2) monolayers. Considering the single-particle dispersion[27] and solving the exciton Wannier equation[10,11,28,29] with a non-local screening in analogy to recent studies,[30] we obtain a set of exciton states $|\alpha\rangle \equiv |\mathbf{Q}, \nu\rangle$ characterized by the valley index ν, the center-of-mass momentum $\mathbf{Q}$ and the exciton energy $\varepsilon_\alpha = E_\nu + \hbar^2|\mathbf{Q}|^2/(2M_\nu)$ with M_ν as the total valley-dependent mass. Due to considerable energy separations, we restrict our attention to the 1s states of the bright excitons (KK) and the momentum-dark excitons (KK′, KΛ) lying approximately 51.5 and 30.5 meV below KK, respectively. These values have been obtained by solving the Wannier equation and are in good qualitative agreement with recent *ab initio* studies.[12] Spin-dark states[20,31] have not been taken into account, as they are not expected to qualitatively affect the main message of this work, *i.e.* the transient spatiotemporal dynamics of spin-allowed states. The former states in fact interact with the latter *via* less-effective carrier-spin-flipping processes.[32,33] Moreover, spin-dark KK states have similar properties to the KK′ excitons (in terms of dispersion relation) and are hence expected to lead at first approximation only to quantitative changes. Furthermore, in this work we focus on the intrinsic undoped regime, where the effect of trions[18,20,34,35] is negligible.

Taking states $|\alpha\rangle \equiv |\mathbf{Q}, \nu\rangle$ as a basis, we introduce the coefficients $\rho_{\alpha\alpha'}$ of the single-particle density matrix[36–38] of incoherent excitons, $\rho_{\alpha\alpha'} = \rho^{\nu\nu'}_{\mathbf{Q}\mathbf{Q}'} = \langle \hat{X}^\dagger_{\alpha'} X_\alpha \rangle$, where $X^{(\dagger)}_\alpha$ are annihilation (creation) operators for the state $|\alpha\rangle$. Then, we introduce the excitonic intravalley Wigner function $N^\nu_\mathbf{Q}(\mathbf{r}, t) \equiv \sum_{\mathbf{q}'} \rho^{\nu\nu}_{\mathbf{Q}-\mathbf{q}'/2,\mathbf{Q}+\mathbf{q}'/2} e^{\imath \mathbf{q}' \cdot \mathbf{r}}$, which summed over $\mathbf{Q}$ provides the intravalley spatial density $N_\nu(\mathbf{r}, t) \equiv \frac{1}{V}\sum_\mathbf{Q} N^\nu_\mathbf{Q}(\mathbf{r}, t)$. The total excitonic density $n_\nu(t)$ in valley ν reads $n_\nu(t) = \int N_\nu(\mathbf{r}, t) \mathrm{d}\mathbf{r} = \sum_\mathbf{Q} \rho^{\nu\nu}_{\mathbf{Q}\mathbf{Q}}$ and is determined by the diagonal density matrix elements. In contrast, the off-diagonal terms induce an explicit dependence on $\mathbf{r}$, *i.e.* they result in a spatial inhomogeneity.

Now, we introduce an equation of motion for the spatiotemporal dynamics of excitons by exploiting the Heisenberg equation and the many-particle Hamilton operator.[28,37,38] The derived semiconductor Bloch equation[10,14] can then be transformed in the Wigner representation[39,40] and reads in the low excitation regime:

$$\partial_\mathrm{t} N^\nu_\mathbf{Q}(\mathbf{r}, t) = \left(\frac{\hbar \mathbf{Q}}{M_\nu} \cdot \nabla - \gamma \delta_{\mathbf{Q},0} \delta_{\nu,KK}\right) N^\nu_\mathbf{Q}(\mathbf{r}, t) + \Gamma^{\nu;KK}_{\mathbf{Q};0} |p_0(\mathbf{r}, t)|^2 + \partial_\mathrm{t} N^\nu_\mathbf{Q}(\mathbf{r}, t)\Big|_\mathrm{scat}. \tag{1}$$

The first term indicates the free evolution of excitons $\nabla_\mathbf{Q} \varepsilon_{\mathbf{Q},\nu} = \hbar\mathbf{Q}/M_\nu$, while the second term takes into account the losses due to the direct photoluminescence $I_\mathrm{PL}(\mathbf{r}, t) = \gamma N^\mathrm{KK}_{\mathbf{Q}\approx 0}(\mathbf{r}, t)$. Here, γ describes the radiative recombination rate within the light cone ($\delta_{\mathbf{Q},0}\delta_{\nu,\mathrm{KK}}$).[10,11,29] The effects of phonon-assisted radiative recombination are beyond the scope of this work.[41]

The first contribution in the second line of eqn (1) describes the formation of incoherent excitons due to phonon-driven transfer from the excitonic polarization $p_{\mathbf{Q}\approx 0}(\mathbf{r}, t)$ (referred to in the literature as coherent excitons[10]). The latter are optically excited by an electromagnetic field $\mathbf{A}(\mathbf{r}, t)$ through $\partial_t p_\mathbf{Q}(\mathbf{r}, t)|_\mathrm{opt} \propto \mathbf{M} \cdot \mathbf{A}(\mathbf{r}, t) \delta_{\mathbf{Q},0}$, with $\mathbf{M}$ depending on optical matrix elements and excitonic wave functions.[10,11] The process is driven by exciton–phonon scattering with the rates $\Gamma^{\nu\nu'}_{\mathbf{Q}\mathbf{Q}'}$ describing scattering from state $|\mathbf{Q}'\nu'\rangle$ to $|\mathbf{Q}\nu\rangle$ *via* interaction with phonons.[10,11] We take into account longitudinal and transverse acoustic (LA, TA) and optical (LO, TO) modes as well as the out-of-plane A_1 optical mode, which provide the most efficient scattering channels.[42] Phonon energies and carrier-phonon scattering coefficients within the deformation potential approximation are extracted from density functional theory studies.[42] Since coherent excitons decay on an ultrafast timescale of 10–100 fs,[10] it is the incoherent exciton distribution that determines the spatiotemporal dynamics of the photoluminescence.

Finally, the last term in eqn (1) describes the scattering contribution. In this work we focus on high-quality hBN-encapsulated TMD monolayer samples, where disorder does not play a large role. The encapsulation with hBN has been applied as a key strategy to prepare high-quality TMD samples, resulting in strong linewidth narrowings,[43,44] ascribed to shielding of the material from the substrate and surface defects as well as to mitigation of the effect of dielectric disorder.[45] We restrict our attention to the low-excitation regime, where the main source of scattering is given by exciton–phonon interactions. The intra- ($\nu = \nu'$) and inter-valley ($\nu \neq \nu'$) contribution can be written as $\partial_\mathrm{t} N^\nu_\mathbf{Q}(\mathbf{r}, t)\Big|_\mathrm{scat} = \sum_{\nu'} \partial_\mathrm{t} N^\nu_\mathbf{Q}(\mathbf{r}, t)\Big|_{\nu'}$, where $\partial_\mathrm{t} N^\nu_\mathbf{Q}(\mathbf{r}, t)|_{\nu'}$

indicates the dynamics of N^{ν} induced by the interaction with $N^{\nu'}$. The corresponding equation of motion reads:

$$\partial_t N_{\mathbf{Q}}^{\nu}(\mathbf{r},t)\Big|_{\nu'} = \sum_{\mathbf{Q}'}\Big[\mathit{\Gamma}_{\mathbf{Q}\mathbf{Q}'}^{\nu\nu'} N_{\mathbf{Q}'}^{\nu'}(\mathbf{r},t) - \mathit{\Gamma}_{\mathbf{Q}'\mathbf{Q}}^{\nu'\nu} N_{\mathbf{Q}}^{\nu}(\mathbf{r},t)\Big], \qquad (2)$$

where the first (second) term describes the in- (out-) scattering dynamics of the Wigner function $N_{\mathbf{Q}}^{\nu}$. Using the index shift $\mathbf{Q} \leftrightarrow \mathbf{Q}'$ one can show for the exciton density $\partial_t N_\nu(\mathbf{r},t)|_{\nu'} \equiv \frac{1}{V}\sum_{\mathbf{Q}} \partial_t N_{\mathbf{Q}}^{\nu}(\mathbf{r},t)\Big|_{\nu'} = -\partial_t N_{\nu'}(\mathbf{r},t)|_{\nu}$. It follows immediately that intravalley scattering does not change $N_\nu(\mathbf{r}, t)$, *i.e.* $\partial_t N_\nu(\mathbf{r}, t)|_\nu = 0$, as expected for broad densities.[46,47] Although having no direct contribution, the intravalley scattering may have a considerable impact on the spatial distribution $N_\nu(\mathbf{r})$, since locally (*i.e.* in every position $\mathbf{r}$) these scattering channels redistribute the Wigner function $N_{\mathbf{Q}}^{\nu}$ in the momentum $\mathbf{Q}$ toward the local equilibrium distribution $N_{\mathbf{Q}}^{\nu o}(\mathbf{r}, t) \propto \exp[-\varepsilon_{\mathbf{Q}\nu}/(k_B T)]$. By studying how the difference between $N_{\mathbf{Q}}^{\nu}$ and $N_{\mathbf{Q}}^{\nu o}$ evolves,[39] it can be shown that the dynamics of the spatial distribution N_ν is given in the absence of intervalley scattering mechanisms and in the steady-state regime by Fick's law

$$\partial_t N_\nu(\mathbf{r},t) = D_\nu \mathit{\Delta}_r N_\nu(\mathbf{r},t). \qquad (3)$$

Here decaying mechanisms have been omitted[18,20] and $D_\nu = 1/2\langle \tau_{\mathbf{Q}}^{\nu} \hbar^2 \mathbf{Q}^2/M_\nu{}^2\rangle|_{\mathbf{Q}}^{\nu}$ is the diffusion coefficient, with $\tau_{\mathbf{Q}}^{\nu} = \sum_{\mathbf{Q}'} \mathit{\Gamma}_{\mathbf{Q}'\mathbf{Q}}^{\nu\nu}$ providing the $\mathbf{Q}$-dependent relaxation time induced by intravalley processes. The introduced expectation value $\langle f_{\mathbf{Q}}\rangle|_{\mathbf{Q}}^{\nu}$ provides the average of $f_{\mathbf{Q}}$ assuming a (local) thermalized distribution $\langle f_{\mathbf{Q}}\rangle|_{\mathbf{Q}}^{\nu} = \sum_{\mathbf{Q}} f_{\mathbf{Q}} \exp\left(-\frac{\varepsilon_{\mathbf{Q}\nu}}{k_B T}\right) / \sum_{\mathbf{Q}} \exp\left(-\frac{\varepsilon_{\mathbf{Q}\nu}}{k_B T}\right)$. Under the assumption of constant relaxation times $\tau_{\mathbf{Q}}{}^{\mathrm{vv}} \approx \tau_\nu$ the well-known steady-state relation $D_\nu = \tau_\nu k_B T/M_\nu$ can be recovered.

The evolution of $N_\nu(\mathbf{r}, t)$ undergoes a so-called *effective diffusion*, *i.e.* (i) it preserves the location of its center (in contrast to transport studies involving a shift of the occupation peak[48]), (ii) it is rotationally symmetric, and (iii) it broadens in space. In order to quantify this effective diffusion process, we introduce a width w_ν of the distribution N_ν which is proportional to the variance, $w_\nu^2 = \int \mathbf{r}^2 N_\nu(\mathbf{r},t)\mathrm{d}\mathbf{r}/n_\nu$. According to Fick's law [eqn (3)], confined spatial distributions would behave as $N_\nu(\mathbf{r}, t) \propto \exp[-\mathbf{r}^2/w_\nu{}^2(t)]$ with $w_\nu^2(t) = w_{\nu,0}^2 + 4D_\nu t$,[17,21] where $w_{\nu,0}^2$ is the initial width. It follows that one can define an *effective diffusion coefficient* (or *diffusivity*) as $D_\nu = \frac{1}{4}\partial_t w_\nu^2$, *i.e.* as the slope of the temporal evolution of the squared width w_ν^2. In the so-called *conventional diffusion*, D_ν is a constant. This behaviour occurs in the steady-state regime and can be described by the conventional Fick's law [eqn (3)]. However, before the steady-state regime is reached, the spatial distribution is expected to undergo a non-trivial evolution, which can be interpreted in terms of a modified Fick's law with a time-dependent effective diffusion coefficient $D_\nu(t)$.[49–51]

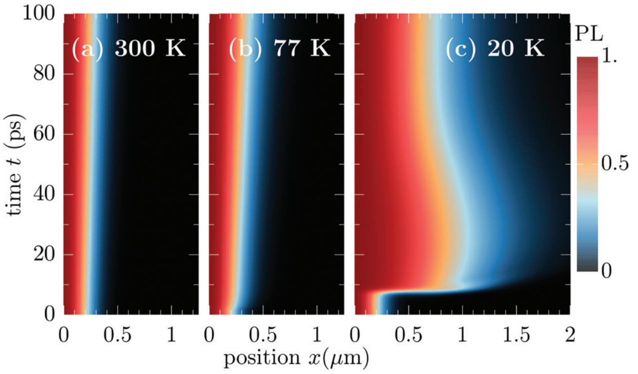

Fig. 2 Normalized photoluminescence in a hBN-embedded monolayer of WS_2 at (a) 300 K, (b) 77 K and (c) 20 K as a function of spatial position x and time t. At the lowest temperature, we observe an unexpected narrowing of the PL spatial distribution indicating a negative effective exciton diffusion. Note that the rotational symmetry around $\mathbf{r} = 0$ is preserved; hence we plot only the values along the x-axis.

As a remarkable example, in the so-called ballistic scenario, where many-particle scattering is negligible, the effective diffusion coefficient $D_\nu(t)$ increases linearly with time t.[25] The intravalley scattering leads the system from a ballistic regime to a conventional diffusion by acting as a frictional mechanism counteracting the free evolution. When the intervalley contribution becomes of the same order of magnitude as the intravalley one, intriguing phenomena are expected including negative effective diffusion effects – as will be discussed below. Since we will mostly focus on transient phenomena, for the sake of simplicity and unless otherwise specified below we will simply write diffusion when referring to effective diffusion.

2. Results

2.1. Spatiotemporal photoluminescence

Now, we exploit the theoretical approach discussed above to describe the spatiotemporal dynamics in monolayer TMDs. First, we create a non-equilibrium through an optical excitation which is resonant to the A exciton and centered in time (around $t_0 = 0.2$ ps with $\mathbf{A}(\mathbf{r}, t)$ having an amplitude FWHM of 100 fs) and space (around $\mathbf{r} = 0$ with amplitude FWHM of 0.5 μm and associated width w of about 0.3 μm). We emphasize that although the size of the intensity affects the initial width of the distribution, its impact on the evolution of $D_\nu(t)$ is found to be negligible, as far as no additional effects induced by stronger localizations are considered.[46,47] Then, we evaluate eqn (1) and (2) to describe transient changes of the effective diffusion coefficients $D_\nu(t)$ including phonon-assisted transfer between bright and momentum-dark excitons.

We start considering the direct PL spatial distribution I_{PL}, which remains rotationally symmetric with respect to its center $\mathbf{r} = 0$, hence we plot only the values along the x-axis. We show in Fig. 2 normalized PL distributions, from which the change of the spatial profile can be better understood, while the unnormalized PL can be found in the ESI.† Note that I_{PL}

undergoes decaying processes similar to the case of spatially homogeneous optical excitation.[10] Such decays are dominated by shape-preserving mechanisms (*e.g.* radiative recombination or fast intervalley thermalization), hence affecting the total exciton density but not the profile of its spatial distribution. While in Fig. 2 the initial shape of I_{PL} follows the intensity of the exciting optical field, its evolution illustrates the increase of the lateral size of the spatial exciton distribution at different temperatures. At 300 K, there is only a modest and constant broadening, while at 77 K, one can see a more pronounced increase of the spatial size due to the weaker counteracting exciton–phonon scattering at lower temperatures. Interestingly, different timescales are observable, exhibiting a much faster effective diffusion in the first few picoseconds followed by a slower broadening.

Further decreasing the temperature to 20 K, we find in addition to an unexpected fast broadening between approximately 4 and 8 ps an even more surprising behaviour: after approximately 30 ps, the PL spatial distribution starts to shrink, *i.e.* the normalized PL profile apparently goes back in space towards the center of the distribution rather than diffusing away from it. This indicates an effective *back-diffusion* (in the sense of reduction of second moment) or according to a modified Fick's law [see eqn (3)], *negative* diffusion. Although also observed in single-species studies,[50,52] negative diffusions appear usually in multi-component systems (also called uphill diffusion, see *e.g.* ref. 53–55). Negative carrier diffusions have been shown *e.g.* in scanning ultrafast electron microscopy studies[56] as a result of spatial separation of electrons and holes and the resulting (Coulomb-induced) interaction. In our case, the multi-component nature is induced by the remarkable multi-valley exciton landscape displayed in TMD monolayers. We will show below that the efficient intervalley exciton–phonon scattering is the origin of both the back-diffusion and the sharp increase at about 4–8 ps. In particular, we will discuss how the observed diffusion delay stems from the interplay of initial valley-intrinsic diffusion (with the appearance of cold/hot energy distribution in bright and dark valleys, respectively) and time required to absorb (acoustic) intervalley phonons from higher-energy dark exciton states.

2.2. Valley-dependent exciton diffusion

To understand the interesting spatiotemporal evolution of the PL, we perform now a quantitative analysis of the shape of excitonic densities including bright and dark states. Fig. 3 illustrates the time evolution of the squared spatial width w_ν^2 and the resulting diffusion coefficient D_ν for KK, KK′ and KΛ excitons. In addition we plot the analogous variables for the total spatial density $N(\mathbf{r}, t)$ obtained by summing over the three intravalley spatial densities $N(\mathbf{r}, t) = \sum_\nu N_\nu(\mathbf{r}, t)$ (dotted lines). The PL (dashed lines) follows the dynamics of N_{KK} while N follows the dynamics of the most occupied valley, *i.e.* KΛ at 300 K and KK′ at the two lowest temperatures. At room temperature [Fig. 3(a)] we observe an almost identical behavior for all three types of excitons. The diffusion coefficients D_ν become very quickly time-independent and reach a stationary value of almost 1 cm^2 s^{-1}. This is the consequence of a very efficient exciton–phonon scattering at 300 K that results in an ultrafast equilibration of all intra- and intervalley exciton states, before a considerable spatial separation between valleys could appear. This is not the case anymore at 77 K [Fig. 3(b)], where we observe valley-dependent values.

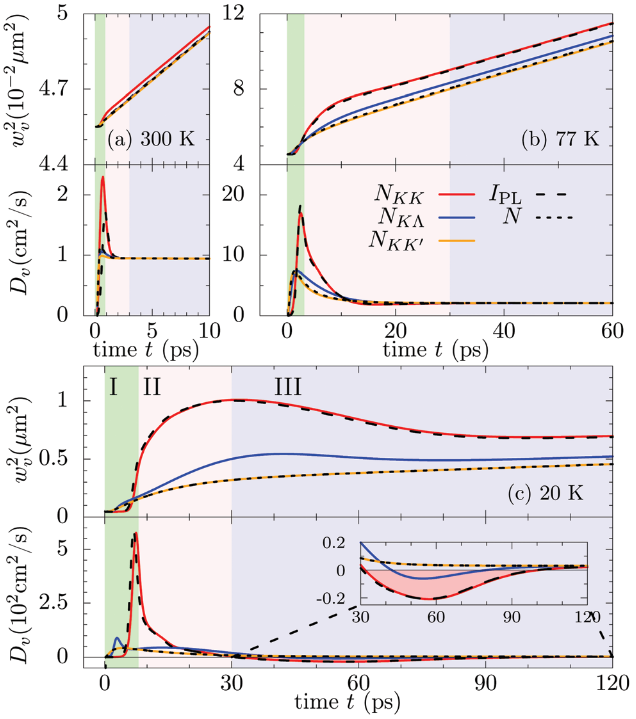

Fig. 3 Temporal evolution of squared spatial width w_ν^2 of excitonic distributions and the associated transient diffusion coefficient D_ν of KK, KK′ and KΛ excitons shown at (a) 300 K, (b) 77 K, and (c) 20 K. The evolution of the direct PL is illustrated with the dashed black line while the one associated with the total spatial density $N(\mathbf{r}, t) = \sum_\nu N_\nu(\mathbf{r}, t)$ is indicated by the dotted black line. The three phases characterizing the spatiotemporal dynamics are denoted with green, red and blue background colors, respectively (as introduced in Fig. 1).

In Fig. 3(b) we find three well-distinguished phases determining the temporal evolution of exciton diffusion in TMD monolayers: (I) an initial phase with a valley-dependent fast increase of diffusion coefficients (green-shaded background), (II) a transient phase where the differences between valleys decrease (red-shaded background), and (III) a final phase, where an effective stationary diffusion coefficient is reached (blue-shaded background). It is the relatively long duration of phase II, where the diffusion coefficients are still valley-intrinsic, that gives rise to the observed different widths w_ν^2 for different exciton densities. These differences are essentially preserved in phase III, *i.e.* the w_ν^2 trajectories tend to be parallel resulting in similar diffusion coefficients D_ν.

Decreasing the temperature to 20 K [Fig. 3(c)], both the maximal values of coefficients D_ν and the spatial separation between valley-dependent widths w_ν^2 further increase, reflecting the strongly reduced efficiency of exciton–phonon scatter-

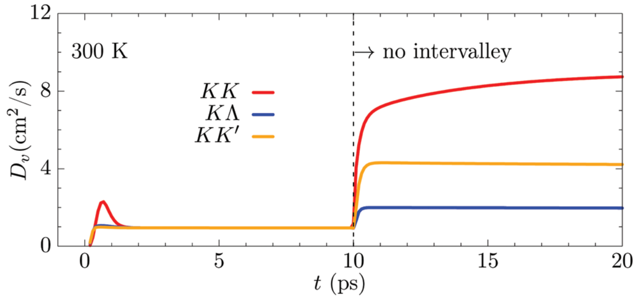

Fig. 4 Diffusion coefficient of KK, KK′ and KΛ excitons at 300 K, where intervalley channels are switched off after 10 ps.

ing counteracting diffusion and valley redistribution of excitons. After the initial steep increase, the diffusion coefficients of both KK and KΛ excitons undergo a subsequent decrease eventually leading to negative values at around 30–100 ps for KK excitons (see the inset). The appearance of negative effective diffusion explains the features observed in the PL in Fig. 2. Although a thorough microscopic description of other interaction mechanisms, such as disorder, has not been considered, we find that on slightly increasing the scattering rates (*i.e.* somehow mimicking the presence of additional scattering channels), the qualitative aspects of the evolution of D_{KK} at 20 K would still be present. Furthermore, in the considered WS_2 monolayer we find that the radiative recombination [see rate γ in eqn (1)] has a negligible effect on D_{KK}. As we will see in the next subsection, the evolution of D_{KK} is in fact ruled by the energetically lowest dark excitonic states, the latter being affected by γ only *via* second order processes (*i.e.* refilling of valley KK).

2.3. Intervalley exciton–phonon scattering

To better understand the mechanism underlying the predicted negative diffusion, we investigate the role of intervalley exciton–phonon scattering. Fig. 4 illustrates the full temporal evolution of D_ν at 300 K in the Gedanken experiments, where we artificially switch off the intervalley scattering after 10 ps. We clearly observe that without intervalley scattering one would have pronounced valley-dependent diffusion coefficients D_ν reflecting different effective masses of the involved valleys. Recalling the discussed steady-state relation between D_ν and intravalley τ_ν, this implies scattering rates of approximately 84 (omitting the radiative decay γ), 66 and 43 fs for KK, KK′ and KΛ excitons, respectively. Fig. 4 already shows the crucial role of intervalley scattering for exciton diffusion even at room temperature.

To be able to quantitatively understand how the intervalley scattering affects the diffusion at low temperatures, we introduce the *scattering-induced shape variation*:

$$\eta_\nu(\mathbf{r},t) = \partial_{\mathrm{t}} N_\nu(\mathbf{r},t)\big|_{\mathrm{scat}} - c_\nu N_\nu(\mathbf{r},t), \tag{4}$$

with the space-independent ratio $c_\nu = \frac{1}{n_\nu}\sum_{\nu'}\int \partial_{\mathrm{t}} N_\nu(\mathbf{r},t)\big|_{\nu'}\mathrm{d}\mathbf{r}$. The shape variation $\eta_\nu(\mathbf{r}, t)$ is the difference between full scattering-induced density dynamics $\partial_{\mathrm{t}} N_\nu(\mathbf{r}, t)|_{\mathrm{scat}}$ and shape-preserving change of exciton amount. The latter only induces a variation of amplitude $N_\nu(\mathbf{r}, t + \Delta t) = (1 + c_\nu \Delta t) N_\nu(\mathbf{r}, t)$ in the limit $\Delta t \to 0$. The quantity η alone, in contrast, would induce $N_\nu(\mathbf{r}, t + \Delta t) = N_\nu(\mathbf{r}, t) + \Delta t\, \eta_\nu(\mathbf{r}, t)$. Since $\int \mathrm{d}\mathbf{r}\, \eta_\nu(\mathbf{r},t) = 0$, it follows that η_ν may describe amount-preserving variations of density N_ν, *i.e.* η_ν extracts the changes in shape of N_ν from $\partial_{\mathrm{t}} N_\nu(\mathbf{r}, t)|_{\mathrm{scat}}$, while the variation of n_ν is described by $c_\nu N_\nu$. The shape variation η_ν describes scattering-induced spatial redistribution of density $N_\nu(\mathbf{r})$ from *e.g.* position $\mathbf{r}_1$ toward $\mathbf{r}_2$ by assuming negative (positive) values in the regions where the distribution is lost (gained). Thus, η directly affects the exciton diffusion process. Exploiting the general definition of the diffusion coefficient D_ν below eqn (3), we introduce a *scattering-induced diffusion coefficient* $D_\nu^{\mathrm{scat}} = \frac{1}{4}\partial_{\mathrm{t}}\left(\langle \mathbf{r}^2\rangle\big|_{\mathbf{r}}^{\nu}\right)\Big|_{\mathrm{scat}} \approx \frac{\int \mathbf{r}^2 \eta_\nu(\mathbf{r},t)\mathrm{d}\mathbf{r}}{\int 4N_\nu(\mathbf{r},t)\mathrm{d}\mathbf{r}}$. This quantity provides the contribution of spatial density redistribution induced by exciton–phonon scattering to the exciton diffusion. Recalling that for broad distributions[46,47] the intravalley scattering mechanisms do not contribute to the scattering-induced dynamics of N_ν, *i.e.* $\partial_{\mathrm{t}} N_\nu(\mathbf{r},t)\big|_{\mathrm{scat}} \equiv \sum_{\nu'} \partial_{\mathrm{t}} N_\nu(\mathbf{r},t)\big|_{\nu'}$, the scattering-induced diffusion coefficient D_ν^{scat} can also be seen as the direct measure for the intervalley scattering-induced diffusion D_ν^{interv}.

Fig. 5(a) shows a direct comparison between scattering-induced ($D_{\mathrm{KK}}^{\mathrm{interv}}$) and full diffusion coefficient D_{KK} at 20 K. We find strong similarities between the two lines, indicating that the scattering-induced diffusion dominates the transient features of D_{KK}. These include *e.g.* the high peak at about 8 ps, which can be explained as follows: due to the low temperature the momentum-dark excitons have not fully thermalized yet, having an overpopulation of states with energies high enough to scatter into KK states (*cf.* blue arrow in Fig. 1(a)).

This can be observed also in Fig. 5(b), where the Wigner distribution $N_{k_x}^{\mathrm{KK}'}(x)$ for KK′ excitons is plotted at 5 ps, *i.e.* during the steep increase. Due to the reduced temperature, both energy and momentum thermalizations are not finished yet. We find a clear anisotropy in momentum, such that there is a higher exciton occupation at positive (negative) momenta for $x > 0$ ($x < 0$). The energy distribution is not thermalized around $k_x \approx 0$, but exhibits peaks at finite momenta indicating a hot exciton distribution.

The non-equilibrium excess-energy is induced by the polarization-to-population transfer, implying that the incoherent dark states formed directly after the optical excitation lay one intervalley phonon energy below the KK minimum (*i.e.* the energy of coherent excitons). This creates an initial hot distribution of dark excitons, which subsequently relaxes toward the corresponding ground state. In contrast, the initial distribution in KK is even colder than 20 K, resulting in a very slow effective diffusion in the bright valley before the steep increase. Note that these hot dark excitons can scatter back into KK exciton states *via* absorption of intervalley phonons.

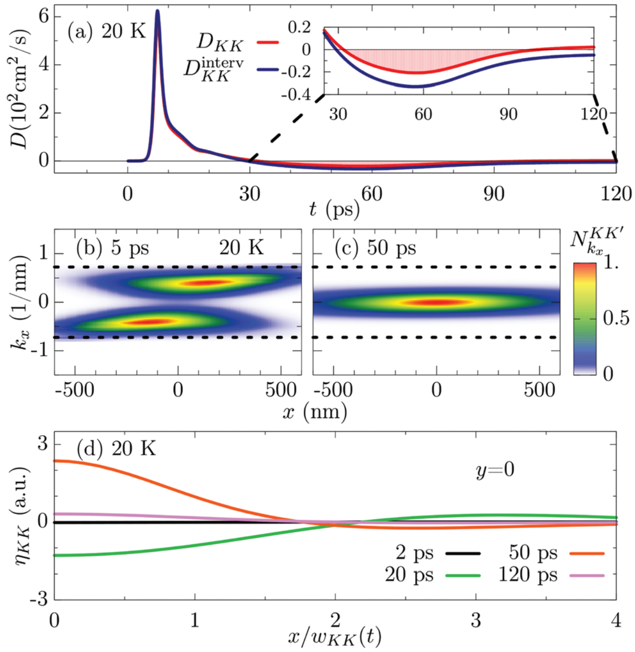

Fig. 5 Illustration of the mechanism behind negative diffusion. (a) Intervalley scattering-induced diffusion coefficient $D_{\text{KK}}^{\text{interv}}$ (see the definition in the text) in direct comparison with the full diffusion coefficient D_{KK} at 20 K illustrating the crucial contribution of intervalley scattering. (b and c) Wigner distribution $N_{k_x}^{\text{KK}'}(x)$ for KK′ excitons plotted at 5 and 50 ps as a function of $\mathbf{k} \equiv (k_x, 0)$ and $\mathbf{r} \equiv (x, 0)$. The dotted line indicates the minimum wave-vector modulus required for the intervalley process into valley KK *via* absorption of acoustic modes. (d) Normalized scattering-induced shape variation [*cf.* eqn (4)] for KK excitons at four different times.

As a guide to the eye, the dotted line in Fig. 5(b and c) indicates the minimum wave-vector modulus required for such an intervalley process *via* absorption of acoustic modes. As shown in Fig. 5(b), the distribution of these KK′ states with high-enough energy is mostly located away from the initial excitation spot, while the other KK′ states with smaller energies are distributed closer to $\mathbf{r} = 0$. Once these spatially wide-spread hot states scatter into KK valley, the density of the latter undergoes a steep extension of its spatial broadening, resulting in the increase of the squared width w_{KK}^2 in Fig. 3(c). The absorption of phonons with finite energy is less effective at small temperatures, thus inducing the time delay of Fig. 2–4, whose duration is found to be directly affected by acoustic-phonon-induced intervalley scattering. Once occupied mostly *via* scattering from high-energy dark states, the KK excitons thermalize. It is during this valley-thermalization phase [*cf.* also Fig. 1 (c and d)] that the negative transient diffusion in D_{KK} appears. When the diffusion of KK excitons shows the highest negative values, the distribution of KK′ excitons is already quasi-thermalized both in energy and momentum, *cf.* Fig. 5(c). It is crucial to have a dark state well below the bright one, so that a hot dark excitonic distribution can be formed giving rise to the steep increase of D_{KK} on a few picosecond timescale, *cf.* Fig. 5(a and b). This behaviour is expected to change qualitatively in semiconductors where the bright exciton is the energetically lowest state.

The driving force behind the remarkable negative diffusion is intervalley exciton–phonon scattering processes, as the similarity of D^{interv} to the scattering-induced diffusion D shows in Fig. 5(a) (see also the inset). Note that the effect of D_{ν}^{interv} becomes smaller for excitons with a higher population, *i.e.*, the energetically lowest and thus the highest occupied KK′ excitons have a negligible D^{interv} (not shown), resulting in a smoother evolution of $w_{\text{KK}'}^2$ and $D_{\text{KK}'}$ [Fig. 3(c)]. In fact, it can be shown that the mutual interaction between two valleys ν_1 and ν_2 leads to $\eta_{\nu_1} \approx -\eta_{\nu_2}$. Inserting the last approximation in the η-dependent definition of D^{interv}, one finds $|D_{\nu_1}^{\text{interv}}| \approx |D_{\nu_2}^{\text{interv}}| n_{\nu_2}/n_{\nu_1}$. As a consequence, for $n_{\nu_1} \ll n_{\nu_2}$ it follows that $|D_{\nu_1}^{\text{interv}}| \gg |D_{\nu_2}^{\text{interv}}|$. This explains why the negative diffusion region only appears for lower-populated exciton valleys [Fig. 3(c)].

The different temporal behaviour displayed by $D_{\text{KK}}^{\text{interv}}$ is induced by different qualitative trends of the shape variation η_{KK}, *cf.* Fig. 5(d). Here, we have normalized η_{KK} with respect to $n_{\text{KK}}(0, t)$ and considered the dimension-free position $x/w_{\text{KK}}(t)$ to compare spatial distributions with different height and width. At 2 ps, the timescale is too short for the absorption of phonons, hence both D^{interv} and η are negligible. In contrast, at 20 ps D^{interv} is very high. Accordingly, η shows the conventional diffusive shape with a transfer of density from the center [$\eta(x) < 0$ for $x \approx 0$] toward the tails ($\eta > 0$ for $x \gtrsim 2w_{\text{KK}}$). However, at 50 ps there is a remarkable change of sign in η, which is now positive in the center and negative in the tail. This implies an uphill transfer of density from the tails toward the center, *i.e.* a negative diffusion, which is in fact displayed in Fig. 5(d) at 50 ps. At 120 ps, there is a similar behaviour of η, however with a reduced magnitude. This implies D^{interv} with a reduced negativity (in agreement with Fig. 5(a)) that is overcompensated for by other mechanisms resulting in an overall positive diffusion, *cf.* the red line in Fig. 5(a).

3. Conclusions

We have shown that the spatiotemporal exciton dynamics in transition metal dichalcogenides can result in an unexpected negative exciton diffusion, *i.e.* a shrinking of the spatial exciton density. Based on a fully quantum mechanical approach providing microscopic insights into time-, momentum- and space-resolved exciton dynamics, we ascribe this behaviour to the interplay of valley-intrinsic diffusion and intervalley thermalization processes. The key ingredient is the remarkable excitonic landscape of TMD monolayers containing bright and lower-lying dark states. Our work sheds light on the emerging field of spatiotemporal dynamics in atomically thin materials and may trigger new experimental and theoretical studies on valley-dependent exciton diffusion.

Conflicts of interest

There are no conflicts to declare.

Acknowledgements

This project has received funding from the Swedish Research Council (VR, project number 2018-00734) and the European Union's Horizon 2020 research and innovation programme under grant agreement no. 785219 (Graphene Flagship).

References

1 T. Mueller and E. Malic, *npj 2D Mater. Appl.*, 2018, **2**, 29.
2 G. Wang, A. Chernikov, M. M. Glazov, T. F. Heinz, X. Marie, T. Amand and B. Urbaszek, *Rev. Mod. Phys.*, 2018, **90**, 021001.
3 D. Xiao, G.-B. Liu, W. Feng, X. Xu and W. Yao, *Phys. Rev. Lett.*, 2012, **108**, 196802.
4 A. Chernikov, T. C. Berkelbach, H. M. Hill, A. Rigosi, Y. Li, O. B. Aslan, D. R. Reichman, M. S. Hybertsen and T. F. Heinz, *Phys. Rev. Lett.*, 2014, **113**, 076802.
5 K. He, N. Kumar, L. Zhao, Z. Wang, K. F. Mak, H. Zhao and J. Shan, *Phys. Rev. Lett.*, 2014, **113**, 026803.
6 H. Yu, X. Cui, X. Xu and W. Yao, *Natl. Sci. Rev.*, 2015, **2**, 57.
7 A. Steinhoff, M. Florian, M. Rösner, M. Lorke, T. O. Wehling, C. Gies and F. Jahnke, *2D Mater.*, 2016, **3**, 031006.
8 G. Wang, C. Robert, M. M. Glazov, F. Cadiz, E. Courtade, T. Amand, D. Lagarde, T. Taniguchi, K. Watanabe, B. Urbaszek and X. Marie, *Phys. Rev. Lett.*, 2017, **119**, 047401.
9 T. Deilmann and K. S. Thygesen, *Phys. Rev. B*, 2017, **96**, 201113(R).
10 M. Selig, G. Berghäuser, M. Richter, R. Bratschitsch, A. Knorr and E. Malic, *2D Mater.*, 2018, **5**, 035017.
11 S. Brem, M. Selig, G. Berghaeuser and E. Malic, *Sci. Rep.*, 2018, **8**, 8238.
12 T. Deilmann and K. S. Thygesen, *2D Mater.*, 2019, **6**, 035003.
13 N. Lundt, L. Dusanowski, E. Sedov, P. Stepanov, M. M. Glazov, S. Klembt, M. Klaas, J. Beierlein, Y. Qin, S. Tongay, M. Richard, A. V. Kavokin, S. Höfling and C. Schneider, *Nat. Nanotechnol.*, 2019, **14**, 770–775.
14 P. Merkl, F. Mooshammer, P. Steinleitner, A. Girnghuber, K. Lin, P. Nagler, J. Holler, C. Schüller, J. Lupton, T. Korn, S. Ovesen, S. Brem, E. Malic and R. Huber, *Nat. Mater.*, 2019, **18**, 691.
15 N. Kumar, Q. Cui, F. Ceballos, D. He, Y. Wang and H. Zhao, *Nanoscale*, 2014, **6**, 4915.
16 S. Mouri, Y. Miyauchi, M. Toh, W. Zhao, G. Eda and K. Matsuda, *Phys. Rev. B: Condens. Matter Mater. Phys.*, 2014, **90**, 155449.
17 J. He, D. He, Y. Wang, Q. Cui, F. Ceballos and H. Zhao, *Nanoscale*, 2015, **7**, 9526.
18 T. Kato and T. Kaneko, *ACS Nano*, 2016, **10**, 9687.
19 L. Yuan, T. Wang, T. Zhu, M. Zhou and L. Huang, *J. Phys. Chem. Lett.*, 2017, **8**, 3371.
20 F. Cadiz, C. Robert, E. Courtade, M. Manca, L. Martinelli, T. Taniguchi, K. Watanabe, T. Amand, A. Rowe, D. Paget, B. Urbaszek and X. Marie, *Appl. Phys. Lett.*, 2018, **112**, 152106.
21 M. Kulig, J. Zipfel, P. Nagler, S. Blanter, C. Schüller, T. Korn, N. Paradiso, M. M. Glazov and A. Chernikov, *Phys. Rev. Lett.*, 2018, **120**, 207401.
22 J. Zipfel, M. Kulig, R. Perea-Causín, S. Brem, J. D. Ziegler, R. Rosati, T. Taniguchi, K. Watanabe, M. M. Glazov, E. Malic and A. Chernikov, arXiv:1911.02909, 2019.
23 M. M. Glazov, *Phys. Rev. B*, 2019, **100**, 045426.
24 R. Perea-Causín, S. Brem, R. Rosati, R. Jago, M. Kulig, J. D. Ziegler, J. Zipfel, A. Chernikov and E. Malic, *Nano Lett.*, 2019, **19**, 7317.
25 F. Steininger, A. Knorr, P. Thomas and S. W. Koch, *Z. Phys. B: Condens. Matter*, 1997, **103**, 45.
26 A. Knorr, F. Steininger, B. Hanewinkel, S. Kuckenburg, P. Thomas and S. W. Koch, *Phys. Status Solidi B*, 1998, **206**, 139.
27 A. Kormányos, G. Burkard, M. Gmitra, J. Fabian, V. Zólyomi, N. D. Drummond and V. Fal'ko, *2D Mater.*, 2015, **2**, 022001.
28 H. Haug and S. W. Koch, *Quantum Theory of the Optical and Electronic Properties of Semiconductors: Fifth Edition*, World Scientific Publishing Company, 2009.
29 M. Selig, G. Berghäuser, A. Raja, P. Nagler, C. Schüller, T. F. Heinz, T. Korn, A. Chernikov, E. Malic and A. Knorr, *Nat. Commun.*, 2016, **7**, 13279.
30 S. Brem, J. Zipfel, M. Selig, A. Raja, L. Waldecker, J. D. Ziegler, T. Taniguchi, K. Watanabe, A. Chernikov and E. Malic, *Nanoscale*, 2019, **11**, 12381–12387.
31 M. R. Molas, C. Faugeras, A. O. Slobodeniuk, K. Nogajewski, M. Bartos, D. M. Basko and M. Potemski, *2D Mater.*, 2017, **4**, 021003.
32 Y. Song and H. Dery, *Phys. Rev. Lett.*, 2013, **111**, 026601.
33 L. Wang and M. W. Wu, *Phys. Rev. B: Condens. Matter Mater. Phys.*, 2014, **89**, 115302.
34 F. Gao, Y. Gong, M. Titze, R. Almeida, P. M. Ajayan and H. Li, *Phys. Rev. B*, 2016, **94**, 245413.
35 M. Titze, B. Li, X. Zhang, P. M. Ajayan and H. Li, *Phys. Rev. Mater.*, 2018, **2**, 054001.
36 F. Rossi and T. Kuhn, *Rev. Mod. Phys.*, 2002, **74**, 895.
37 M. Kira and S. W. Koch, *Prog. Quantum Electron.*, 2006, **30**, 155.
38 E. Malic and A. Knorr, *Graphene and Carbon Nanotubes: Ultrafast Optics and Relaxation Dynamics*, Wiley, John & Sons, 2013.
39 O. Hess and T. Kuhn, *Phys. Rev. A*, 1996, **54**, 3347.
40 R. Jago, R. Perea-Causín, S. Brem and E. Malic, *Nanoscale*, 2019, **11**, 10017.
41 S. Brem, A. Ekman, D. Christiansen, F. Katsch, M. Selig, C. Robert, X. Marie, B. Urbaszek, A. Knorr and E. Malic, arXiv:1904.04711, 2019.
42 Z. Jin, X. Li, J. T. Mullen and K. W. Kim, *Phys. Rev. B: Condens. Matter Mater. Phys.*, 2014, **90**, 045422.

43 F. Cadiz, E. Courtade, C. Robert, G. Wang, Y. Shen, H. Cai, T. Taniguchi, K. Watanabe, H. Carrere, D. Lagarde, M. Manca, T. Amand, P. Renucci, S. Tongay, X. Marie and B. Urbaszek, *Phys. Rev. X*, 2017, **7**, 021026.

44 O. A. Ajayi, J. V. Ardelean, G. D. Shepard, J. Wang, A. Antony, T. Taniguchi, K. Watanabe, T. F. Heinz, S. Strauf, X.-Y. Zhu and J. C. Hone, *2D Mater.*, 2017, **4**, 031011.

45 A. Raja, L. Waldecker, J. Zipfel, Y. Cho, S. Brem, J. D. Ziegler, M. Kulig, T. Taniguchi, K. Watanabe, E. Malic, T. F. Heinz, T. C. Berkelbach and A. Chernikov, *Nat. Nanotechnol.*, 2019, **14**, 832–837.

46 R. Rosati and F. Rossi, *Appl. Phys. Lett.*, 2013, **103**, 113105.

47 R. Rosati and F. Rossi, *Phys. Rev. B: Condens. Matter Mater. Phys.*, 2014, **89**, 205415.

48 R. Rosati, F. Lengers, D. E. Reiter and T. Kuhn, *Phys. Rev. B*, 2018, **98**, 195411.

49 D. F. Cordovilla Leon, Z. Li, S. W. Jang, C.-H. Cheng and P. B. Deotare, *Appl. Phys. Lett.*, 2018, **113**, 252101.

50 H. Zhao, B. D. Don, S. Moehl, H. Kalt, K. Ohkawa and D. Hommel, *Phys. Rev. B: Condens. Matter Mater. Phys.*, 2003, **67**, 035306.

51 D. F. Cordovilla Leon, Z. Li, S. W. Jang and P. B. Deotare, arXiv:1908.07648, 2019.

52 H. Zhao, B. D. Don, G. Schwartz and H. Kalt, *Phys. Rev. Lett.*, 2005, **94**, 137402.

53 P. K. Gupta and A. R. Cooper, *Physica*, 1971, **54**, 39.

54 M. B. Wolf and D. London, *Geochim. Cosmochim. Acta*, 1994, **58**, 4127.

55 A. Lauerer, T. Binder, C. Chmelik, E. Miersemann, J. Haase, D. M. Ruthven and J. Kärger, *Nat. Commun.*, 2015, **6**, 7697.

56 E. Najafi, A. Jafari, B. Liao and A. Zewail, arXiv:1909.06338, 2019.